ChemistrySelect

Research Article
doi.org/10.1002/slct.202300708

Chemistry Europe
European Chemical Societies Publishing

www.chemistryselect.org

Green Synthesis of Metal Nanoparticles and Magnetic Nanocomposites for Adsorption, Desorption and Preconcentration of Pb(II)

Muradiye Şahin[b] and Yasin Arslan*[a]

Synthesis, characterization, Pb(II) adsorption, recovery, preconcentration and reusability of different nanoadsorbents were investigated in detail. With green synthesis, silver, iron oxide and iron copper nanoparticles (AgNPs, Fe_3O_4NPs and Fe/CuNPs) were synthesized and modified with chitosan and alginate natural polymers to form nanocomposite beads (Fe_3O_4-CS, Fe_3O_4–AT, Fe/Cu–CS and Fe/Cu–AT). When the adsorption efficiencies of the seven synthesized nanoadsorbents from the aqueous medium were compared, it was seen that the magnetic bimetallic Fe/Cu–CS beads provided the highest adsorption with 100% efficiency for Pb(II). The adsorption mechanism, effects of temperature, initial lead ion concentration and pH of the solution on the Pb(II) adsorption capacity of Fe/Cu–CS beads were investigated. The recovery studies have shown that Fe/Cu–CS beads have good adsorption/desorption performance around 90% of desorption was achieved with 5 mM HNO_3. These results show that Fe/Cu–CS beads have potential to be a promising material for adsorption, preconcentration and desorption of Pb(II) from aqueous solution.

Introduction

Heavy metals, which enter the human body mostly through nutrition and air, are not biodegradable and cause toxic effects by accumulating in living organisms.[1] With the rapid progress of industrial activities in recent years, the use of heavy metals has increased and the pollution resulting from this use has reached the environment, water and especially the food chain.[2] In people exposed to heavy metals in greater than tolerable levels; some problems such as cancer, anemia, respiratory diseases, stomach disorders, damage to brain tissues, kidney failure, high blood pressure, and behavioral disorders due to mental and neurological effects have been observed.[3–6] Lead (Pb), a heavy metal, can be found in the wastewater of various industrial establishments. It can be mixed in water environments from battery industries, mining industries, metal electroplating, painting and coating, journalism and casting processes[7,8] and battery industries lead the way with 5–66 mg/L level.[9] When the health effects of it are examined, even in low dosages, it can cause various effects, such as miscarriage risk in humans, kidney diseases, anemia, hypertension, brain damage, mental retardation, anorexia and fatigue, as well as plant and animal deaths.[10,11]

For these reasons, Pb and other heavy metals that reach the drinking water and food chain as a result of industrial activities should be removed from wastewater before discharge. As treatment techniques used to remove heavy metal ions from the water environment; some methods, such as chemical precipitation, filtration, chemical oxidation, ion exchange, using microorganisms, reverse osmosis, flotation, activated sludge systems and adsorption are used.[12–19] The adsorption method in the removal of heavy metal ions from wastewater is very interesting in terms of its efficiency, low cost and ease of application.[20] Today, the development and use of innovative, environmentally friendly, low-cost adsorbents is of great importance for the adsorption method and various studies are carried out in this direction. Nanoparticles are used as adsorbents to increase the capacity in wastewater treatment due to their high surface area and active adsorption sites that strengthen their interaction with metallic species.[21,22]

During heavy metal removal processes, adding magnetic properties to nanoparticles facilitates the separation of problematic sludges which have high heavy metal content from water, due to their magnetic properties. Therefore, magnetic nanoparticles are an alternative adsorbent material that can be used instead of costly materials used in processes, such as activated carbon, membrane filtration and ion exchange.[23,24] In general, some factors, such as the usage area and removal efficiency of the nanoparticle vary according to the synthesis method. Many methods, such as co-precipitation, thermal decomposition, microemulsion, hydrothermal method and sonochemical synthesis are used in the synthesis of nanoparticles, and changes, such as coating, complex, and hybrid formation can be made on the nanoparticle surface during or after synthesis.[25–30] Different nanomaterials can effectively remove heavy metal from water, but their agglomeration limits their use. However, the agglomeration problem can be minimized by converting nanomaterials into polymer-based

[a] *Y. Arslan*
Department of Nanoscience and Nanotechnology
Faculty of Arts and Science
Burdur Mehmet Akif Ersoy University
Burdur 15030, Turkey
E-mail: yasinarslan@mehmetakif.edu.tr
[b] *M. Şahin*
Institute of Science
Kırşehir Ahi Evran University
Kırşehir 40100, Turkey

Supporting information for this article is available on the WWW under https://doi.org/10.1002/slct.202300708

nanocomposites.[31,32] It was found that bimetal magnetic nanomaterials (Fe–Mn, Fe–Cu, Fe–Ce etc.) showed higher adsorption capacity for heavy metal than single metal magnetic nanomaterials.[33,34] Bimetal magnetic nanomaterials adsorb heavy metals from wastewater by a combination of binding, magnetic selective adsorption, electrostatic interaction and modified ligands.[35]

In this study, AgNPs, Fe_3O_4NPs and Fe/CuNPs nanoparticles were synthesized by green synthesis method using an endemic lathyrus brachypterus plant extract and they were modified with natural polymer, such as chitosan and alginate to form Fe_3O_4–CS, Fe_3O_4–AT, Fe/Cu–CS and Fe/Cu–AT magnetic beads. The all synthesized nanoparticles and nanocomposites were used as adsorbents to investigate the adsorption and desorption of Pb(II) from mg/L to ng/mL level in aqueous solution. The effects of ambient conditions on removal efficiency, desorption and reusability properties were investigated with the nanoadsorbent providing the highest removal. In addition, kinetic, isotherm and thermodynamic parameters were also investigated in detail.

Results and discussion

Preparation of Lathyrus Brachypterus Plant Extract

Lathyrus Brachypterus Plant was firstly homogenized to obtain powder. To obtain its extracts, 2 g of the particular powder was added to 100 mL of distilled water. The mixture was stirred continuously at 25 °C for 5 hours. After grinding, the solution was filtered through a filter paper. Then, all extracts were stored at room temperature to be used for both the characterization and biosynthesis of silver and magnetic nanoparticles.

Synthesis of AgNPs

To prepare AgNPs, 5 mL of extract was mixed with 0.1 M, 45 mL of $AgNO_3$. Then, the mixture was left at room temperature with magnetic stirrer to efficiently complete the synthesis of AgNPs in which plant extract acted as both stabilizer and reductant. After the reduction of Ag^+ ions to Ag^0 were completed for about 5–6 minutes, the AgNPs were filtered through a Whatman No 1 filter paper (90 mm, 82 g/m^2 and pore size: 15–19 μm).[36]

Synthesis of Fe_3O_4NPs and Fe/CuNPs

For the synthesis of Fe_3O_4NPs, 100 mL solution including 0.56 g $FeSO_4 \cdot 7H_2O$ and 0.81 g $FeCl_3 \cdot 6H2O$ was prepared and 10 mL of the plant extract was added to the prepared solution. For the synthesis of Fe/CuNPs, 100 mL solution including 1.38 g $FeSO_4 \cdot 7H_2O$ and 0.18 g $CuSO_4 \cdot 5H_2O$ was prepared and 10 mL of the plant extract was added to the prepared solution. Then, they were mixed at room temperature for 30 min at 500 rpm on a magnetic stirrer and left to settle. The resulting Fe_3O_4 and Fe/Cu nanoparticles were separated from the filtrate with a magnet and washed 3 times with distilled water and dried in an oven.[37,38]

Synthesis of Fe3O4-CS and Fe/Cu–CS

0.50 g of chitosan was mixed with 50 mL of 1% acetic acid until a homogeneous mixture was obtained. Then, 0.40 g of the synthesized magnetic Fe_3O_4NPs was added to this mixture and dropped into 100 mL of 1 M NaOH solution with a dropper to form Fe_3O_4–CS beads. The formed beads were kept in NaOH for 12 hours and washed with distilled water. At the end of the period, half of them were kept in distilled water at 4 °C, and the other half was dried in an oven at 50 °C to compare their adsorption and oxidation effects separately. The same process was performed by replacing Fe_3O_4NPs with Fe/CuNPs for the synthesis of Fe/Cu–CS.[37,38]

Synthesis of Fe_3O_4–AT and Fe/Cu–AT

0.60 g of sodium alginate was mixed with 50 mL of distilled water until a homogeneous solution was formed. 0.50 g Fe_3O_4NPs was added to the prepared mixture and sonicated for 30 minutes. Then, Fe_3O_4–AT beads were formed by dropping the obtained homogeneous solution into 2% of $CaCl_2$ solution. The obtained beads were washed with distilled water and stored into distilled water at 4 °C. The same process was performed by replacing Fe_3O_4NPs with Fe/CuNPs for the synthesis of Fe/Cu–AT.[37,38]

Characterization of nanoparticles and nanocomposites

Based on the characterization results shown in Figures S1–S4 for AgNPs and shown in Figures S5–S8 for both magnetic nanoparticles and nanocomposites; it was confirmed that nanoparticles and nanocomposites were successfully synthesized. UV-Vis spectra of both plant extract and AgNPs were given in Figure S1. The UV-Vis spectral analysis, the characteristic absorbance peak at about 452 nm is commonly used for the definition of AgNPs.[36] FT-IR analyzes of both plant extract and AgNPs were performed and given in Figure S2 as comparatively. In the FT-IR spectra of plant extract, –OH peak was observed at 3285 cm^{-1}. The peak observed at 2973 cm^{-1} corresponds to N–H bond, the peak observed at 1650 cm^{-1} corresponds to C=C double bonds or aromatic rings, and the peak observed at 1420 cm^{-1} corresponds to C=O stretching in the carboxyl group. The peak observed at 1026 cm^{-1} corresponds to the stretching of the amines – CN – and the peak observed at 602^{-1} corresponds to the C–H vibration. The peak observed at 1307 cm^{-1} may be associated with geminal methyl. FT-IR results prove the presence of alkaline, methylene, alkene, amine, phenol and carboxyl groups in the plant extract. These chemical groups have proved to be reducing agents that assist in the synthesis of AgNPs.[39,40] When FT-IR spectra of both the plant extract and AgNPs are compared, it is seen that the peak intensities are either very weak or completely lost in the AgNPs spectra with respect to the plant extract spectra suggesting that the endemic plant used for the first time, is an effective reducing agent for the synthesis of AgNPs. In order to determine the crystal structure of the synthesized AgNPs, XRD analysis was performed and the XRD measurement result was

given in Figure S3. As a result of the obtained diffraction patterns, peaks belonging to (111), (200), (220) and (311) crystal structures were observed corresponding to the angle values of $2\theta = 38.1°$, 44.3°, 64.4° and 77.5° for metallic silver (JCPDS 04–0783). From these results, it was understood that there was a metallic silver in a face-centered cubic structure. In addition, it was concluded from the diffraction patterns that the metals from the plant were found as impurities. In this part of study, particle sizes of AgNPs were calculated using the Scherrer equation from the XRD results.

Calculation of D_{111} particle size using the Scherrer equation (1);

$$D_{111} = \frac{k\lambda}{(\beta cos\theta)} \quad (1)$$

in which D111 is the particle size (nanometers), $k = 0.94$ is the constant associated with the crystal shape, β is the measure of the full width of half height of the peak at the maximum intensity (in the 111 plane) in the spectrum, λ is the X-ray wavelength, and θ is the angle of the diffraction peak (Bragg). The average particle size of AgNPs found in the calculation with the characteristic Ag (111) peak was found to be 6.08 nm. TEM analyses were also performed to observe the geometric properties, particle size and distribution of the synthesized AgNPs. It is observed in Figure S4 that AgNPs are formed properly, they are in crystalline structure and there is no big difference between their sizes. In addition, from the size distribution histogram in Figure S4, it is seen that the nanoparticle size varies between 6 nm and 30 nm; the average size of the particles was found to be 14.15 ± 0.20 nm. As seen, there is a good agreement with the particle sizes calculated by the Scherrer equation in the XRD spectra shown in Figure S3.

The peaks seen in UV-Vis. (Figure S5a) are the characteristic peaks of Fe_3O_4NPs and Fe/CuNPs and it was confirmed that the nanoparticles were successfully synthesized.[41,42] The pHpzc values of Fe_3O_4NPs, Fe_3O_4–CS, Fe_3O_4–AT, Fe/CuNPs, Fe/Cu–CS and Fe/Cu–AT were found to be 6.47; 5.18; 5.65; 6.32; 5.54 and 5.87, respectively (Figure S5b). The studies were carried out at $pH = 6$, which is above the pzc value nearly for all adsorbents. If the pH is above the pHpzc value, the surface charge of the adsorbent becomes negative, so cations can be adsorbed.[43] Since heavy metals precipitate as insoluble hydroxides at high pH, pH 6 was chosen as the optimum value. FTIR results of Fe/CuNPs, Fe/Cu–CS, Fe/Cu–AT, Fe_3O_4NPs, Fe_3O_4–CS, Fe_3O_4–AT and L. Brachypterus extract are given comparatively in Figure S6a. The characteristic peak at 555 cm^{-1} seen in all nanoparticles FT-IR spectra is due to the stretching vibration of the Fe–O bond[44,45] and the characteristic peak at 1008 cm^{-1} is due to the presence of Cu.[46] The peak seen at 3465 cm^{-1} in the FT-IR spectrum of both Fe/Cu–CS and Fe_3O_4–CS belongs to the –NH or –OH asymmetric vibration of chitosan. The width of this peak is due to the presence of hydrogen bonding in the nanocomposite. An H bond is formed by attaching the –NH or –OH group of pure chitosan to the –OH group of acetic acid.[47] Apart from these, the stretching vibration of C=O at 1732 cm^{-1}, the C–O–C bonds of the polysaccharide skeleton at 1028 cm^{-1} and the characteristic peaks of β-1,4-glycosidic bond at 1153 and 895 cm^{-1} show that chitosan is present in the structure.[48] In the FT-IR spectrum of both Fe/Cu–AT and Fe_3O_4–AT, O–H stretches at 3313 cm^{-1}, asymmetric and symmetrical stresses due to –COO at 1595 and 1417 cm^{-1}, –O–C–O– stretches of ether groups and –C–O– stretches of alcohol groups at 1100−1300 cm^{-1} indicate that there is alginate in the structure.[49–51] The X-ray diffraction patterns of Fe/CuNPs, Fe/Cu–CS, Fe/Cu–AT, Fe_3O_4NPs, Fe_3O_4–CS and Fe_3O_4–AT magnetic nanoparticles are shown in Figure S6b. In the XRD pattern of Fe/CuNPs, 4 peaks corresponding to $2\theta = 37.4$, 44.6, 57.8 and 61.4 angle values belong to $CuFeO_2$, zero-valent iron (Fe^0), Fe_2O_3 and Cu_2O, respectively.[52–55] The particle size of Fe/CuNPs was calculated as 18.05 nm from the Debye-Scherrer equation using the peak intensity observed at $2\theta = 37.4$ in the diffraction pattern of these nanoparticles. In the XRD pattern of Fe_3O_4NPs, 6 peaks belonging to the crystal structures 220, 311, 400, 422, 511 and 440 were observed, corresponding to the angle values of $2\theta = 30.18$, 35.47, 43.30, 53.42, 57.18 and 62.70 (JCPDS 65–3107). The particle size of Fe_3O_4NPs was calculated as 11.02 nm from the Debye-Scherrer equation using the peak intensity observed at $2\theta = 35.47$ in the diffraction pattern of these nanoparticles. The 4 peaks detected in the XRD pattern of Fe/CuNPs were also detected in the diffraction pattern of both Fe/Cu–CS and Fe/Cu–AT nanocomposites and 6 peaks detected in the XRD pattern of Fe_3O_4NPs were also detected in the diffraction pattern of both Fe_3O_4–CS and Fe_3O_4–AT nanocomposites. This result showed that the coating of both Fe/CuNPs and Fe_3O_4NPs with chitosan and alginate did not change the crystal structure. The shape and size of the Fe_3O_4NPs were additionally characterized by TEM and SEM-EDX analysis (Figure S7). The SEM images show individualistic Fe_3O_4NPs besides a series of aggregates (Figure S7a). The map data of elemental mapping confirmed the presence of Fe and O and is consistent with the SEM images (Figure S7c). The EDX spectra of Fe_3O_4NPs reveals that there are both Fe and O atoms in its structure (Figure S7c). TEM images (Figure S7b) obviously shows that the nanoparticles are nearly spherical in shape. Figure S7b also indicates the size distribution histogram of the particles and while the sizes of the nanoparticles vary among 5 nm and 42 nm, the mean size of the particles is found to be 11.02 ± 0.15 nm. As seen, there is a good agreement with the particle sizes calculated by the Scherrer equation in the XRD pattern shown in Figure S6b. The shape and size of the Fe/CuNPs were also determined by TEM and SEM analysis (Figure S8). The SEM images show individualistic Fe/CuNPs besides a series of aggregates (Figure S8b). The map data of elemental mapping confirmed the presence of Fe and Cu and is consistent with the SEM images (Figure S8(b,c)). In addition, as seen from the EDX analysis results (Figure S8d), it was confirmed that the bimetallic nanoparticle was synthesized with 58.06% Fe and 35.76% Cu in the structure. TEM images (Figure S8a) obviously show that the nanoparticles are nearly spherical in shape. Figure S8a also indicates the size distribution histogram of the particles and the mean size of the particles is found to be 18.05 ± 0.04 nm and the size of the nanoparticles varies between 6 and 30 nm and showed supermagnetic property.[24,56]

Adsorption performances of Pb(II) onto nanoadsorbents

The removal of Pb(II) from the both synthetic and tap water samples by adsorption on nanoparticles (AgNPs, Fe_3O_4NPs and Fe/Cu NPs) and nanocomposites (Fe_3O_4–CS, Fe/Cu–CS, Fe_3O_4–AT and Fe/Cu–AT) using the batch adsorption method was investigated. For this, a stock solution of 1000 mg/L $Pb(NO_3)_2$ was prepared. Then, this solution was diluted to prepare all other Pb(II) standard solutions. During adsorption, 0,025 g adsorbent was separately contacted with 25 mL 20 mg/L, 50 ng/L and 200 ng/mL Pb(II) solutions in a 50 mL plastic centrifuge tubes. The tubes were then capped and shaken on a magnetic stirrer at 250 rpm at room temperature for 24 h. Solution pH was initially adjusted to 6. Afterwards, the concentration of them remaining without being adsorbed in the solution was determined by both AAS and ICP-OES instruments.

The amount of adsorbed Pb(II), q_e (mg/g), was calculated by equation (2):

$$q_e = \frac{(C_0 - C_e)\ V}{W} \quad (2)$$

where C_0 and C_e are the initial and equilibrium concentrations (mg/L), respectively, V is the volume of Pb(II) solution (L), and W is the weight (g) of nanoadsorbent.

According to the experimental results, Pb removal % of AgNPs, Fe/CuNPs, Fe_3O_4NPs, Fe_3O_4–CS, Fe/Cu–CS, Fe/Cu–AT and Fe_3O_4–AT was found to be 98%, 96%, 95%, 98%, 100%, 98% and 92%, respectively. it was seen that the most suitable adsorbent was found to be Fe/Cu–CS nanocomposite which adsorbed 100% with a maximum monolayer adsorption capacity of 20 mg/g at 298 K shown in Figure 1.

To measure the effect of other ions on Pb(II) removal, the experiment was repeated with tap water and it was observed that other ions in the environment had no significant interference effects.

Effect of initial Pb(II) concentration

The effect of the initial Pb(II) concentration on the adsorption amount was investigated by changing the Pb(II) concentration in the range of 20, 50 and 100 mg/L and the results are given in Figure 2. As seen in the Figure 2, the initial concentration of Pb(II) actually affects the adsorption process. When the concentration increases from 20 mg/L to 50 mg/L, the adsorption capacity increases rapidly, and when the concentration is increased from 50 mg/L to 100 mg/L, there is a decrease in the increase in adsorption capacity. At high Pb(II) concentrations, a concentration gradient, which is a driving force for adsorption, occurs, which increases the qe value.[57] According to the Langmuir model, as seen in the isotherm curve in Figure 5, the maximum adsorption capacity reaches 61.5 mg/g at a concen-

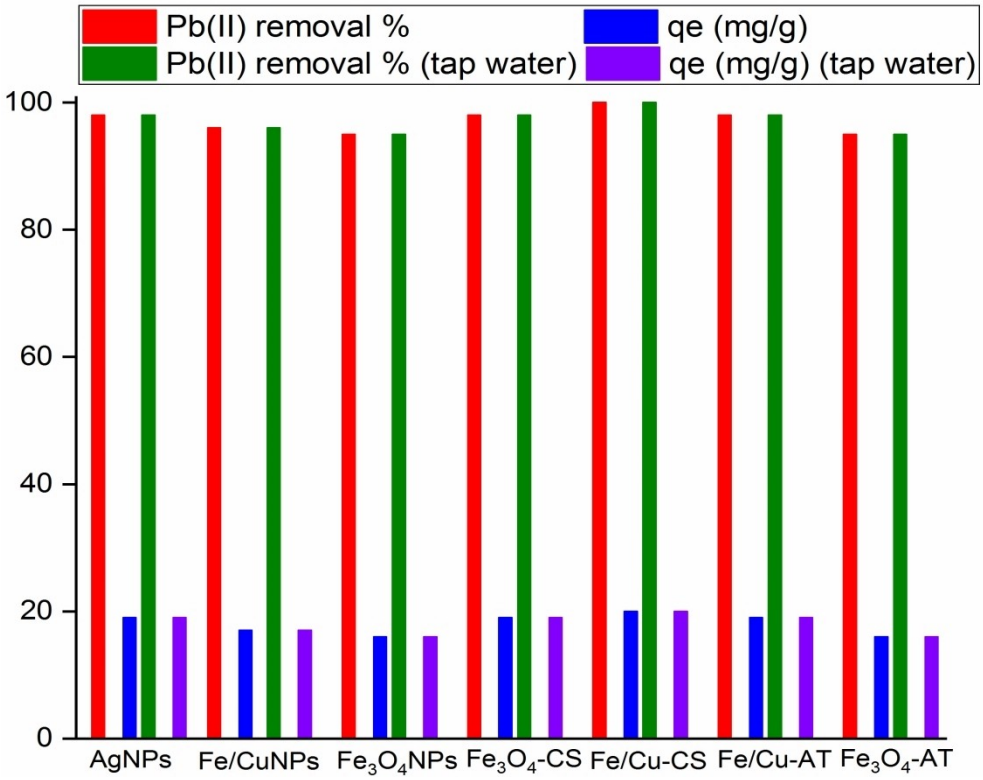

Figure 1. Comparative Pb(II) adsorption of AgNPs, Fe_3O_4NPs, Fe_3O_4–CS, Fe_3O_4–AT, Fe/CuNPs, Fe/Cu–CS and Fe/Cu–AT removal efficiency (initial Pb(II) concentration: 20 mg/L, adsorbent dosage: 25 mg/25 mL, T = 298 K, pH = 6.5).

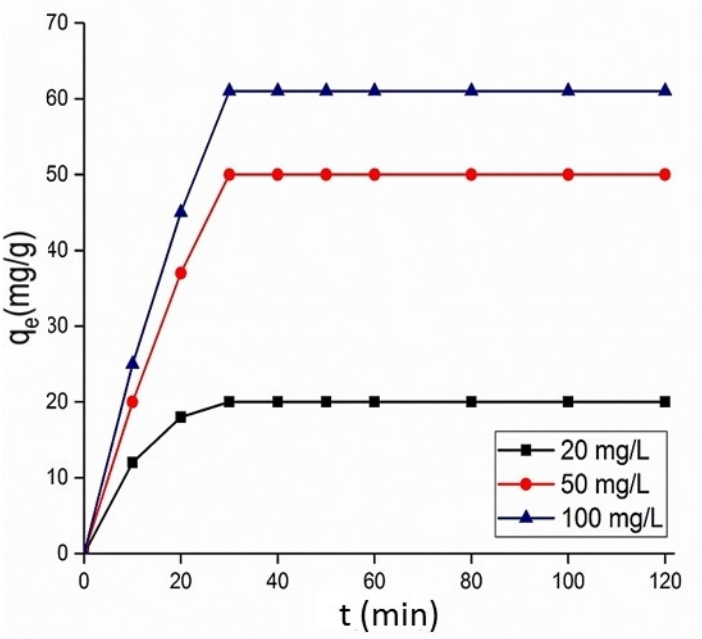

Figure 2. Effect of initial Pb(II) concentration on the Pb(II) adsorption (adsorption conditions: adsorbent dosage: 25 mg/25 mL, pH = 6, T = 298 K, shaking rate 250 rpm and 120 min.).

tration of approximately 100 mg/L at 298 K, and the increase in the concentration after this concentration does not affect the adsorption capacity. This can be explained by the depletion of all active sites on the adsorbent surface. It can also be explained by the fact that Fe/Cu–CS bimetallic nanocomposite forms a passivation layers, such as (PbOH), Cu–Pb-(oxy)hydroxide or Fe–Pb (oxy)hydroxide with Pb.[58,59]

Effect of pH

To investigate the effect of ambient pH on the adsorption of Pb(II) ions, 25 mL, 20 mg/L Pb(II) was separately prepared at pH 3, 5, 6, 8 and 10. Then, 25 mg of synthesized Fe/Cu–CS nanoadsorbent was separately added to these solutions. To examine at which pH value, the adsorption was more effective, the resulting mixture was stirred in a magnetic stirrer for 30 minutes. pH values were adjusted using NaOH and HCl shown in Figure 3. Although the adsorption of metal ions from aqueous solution involves quite complex mechanisms, it is thought that the predominant type of interaction is the electrostatic interaction between the metal ion and the adsorbent surface. As the pH value of the aqueous solution decreases, that is, as an acidic environment occurs, the surface functional groups become positively charged because the adsorbent is surrounded by H_3O^+ ions. Since Pb(II) ions are also cationic in aqueous solution, H_3O^+ ions at acidic pH values prevent Pb(II) cations from approaching the adsorbent due to electrostatic repulsion. Therefore, it is observed that the Pb(II) adsorption efficiency is low at acidic pH values (Figure 3). As the pH value of the aqueous solution increases, the competitive effect of H_3O^+ ions with Pb(II) ions to adhere to the active sites

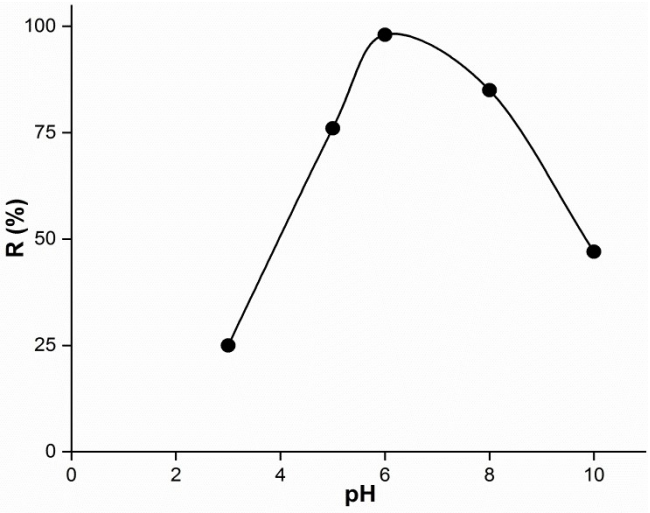

Figure 3. Effect of pH on the Pb(II) adsorption (adsorption conditions: initial Pb (II) concentration: 20 mg/L, adsorbent dosage: 25 mg/25 mL, T = 298 K, and 30 min.).

on the adsorbent surface decreases, and the Pb(II) adsorption efficiency increases as a result of the increase in electrostatic interaction due to the decrease in the positive charge density on the Fe/Cu–CS bead surface.[60,61] The pH effect is closely related to the pHpzc value of the adsorbent. The pHpzc value of the Fe/Cu–CS bead was determined as 5.54 (Figure S5b). When the pH value of the aqueous solution is lower than 5.54, the net surface charge of the adsorbent is positive, and above this value it is negative. As can be seen from Figure 3, the adsorption efficiency for Pb(II) ions is the highest around pH 6.

After pH 6.0, the adsorption efficiency tended to decrease and the optimum pH value at which the maximum removal efficiency was obtained was determined as 6.0, taking into account the precipitation of Pb(II) cations as hydroxides at higher pH values.

Effect of temperature

The effect of temperature for Pb (II) adsorption on Fe/Cu–CS beads was investigated at 298, 313 and 328 K and Pb (II) removal efficiency with time is given in Figure 4. It was observed that the adsorption increased with increasing temperature. This suggests that adsorption is controlled by an endothermic process. The reason for the increase in adsorption capacity with increasing temperature is because the diffusion rate of Pb(II) ions increases with increasing temperature and the mobility of Pb(II) molecules increases, resulting in more interactions with active centers on the surface.[62]

Adsorption isotherms

Adsorption isotherm experiments were performed at different temperatures (298, 313 and 328 K) for 120 minutes with a concentration ranging from 2 to 1000 mg/L Pb(II) initial concentrations. Equilibrium values for Pb(II) cation in solid and liquid phases reached at different initial concentrations are shown in Figure 5. The model parameters were determined as a result of nonlinear regression analysis of the experimental equilibrium data and are listed in Table 1. According to the regression coefficients, it was seen that the Langmuir isotherm model equation describes the experimental equilibrium data better than the other models.

With the increase of Pb(II) ion concentration up to the adsorption saturation limit, the removal capacity increased rapidly. With the increase of Pb(II) ion concentrations, the removal rate firstly slowed down due to the saturation of the Fe/Cu–CS surface and remained stable after reaching equilibrium. According to Langmuir isotherm model; it is based on the idea that the adsorbent surface is homogeneous, there is no interaction between the adsorbed molecules, and there is a fixed number of active sites with the same energy on the adsorbent. This model is expressed by equation (3).

Table 1. Modeling the experimental data of Pb(II) adsorption onto the Fe/Cu–CS adsorbent with the corresponding parameters of the isotherm models.

Model Parameters		Unit	Solution Temperature		
			298 K	313 K	328 K
Langmuir	q_m	mg/g	61.5	63	66
	K_L	L/mg	0.064	0.069	0.087
	R^2	–	0.9988	0.9993	0.9984
Freundlich	K_F	(mg/g)*(mg/L)^n	4.125	4.018	4.107
	n	–	0.75	0.77	0.82
	R^2	–	0.9124	0.9276	0.8961
Temkin	B	J/mol	−23.50	−21.37	−19.78
	K_T	L/mg	0.0019	0.0013	0.0009
	R^2	–	0.9581	0.9608	0.9549

$$q_e = \frac{q_m K_L C_e}{1 + K_L C_e} \quad (3)$$

According to Freundlich isotherm; it is taking into account the multilayer adsorption and heterogeneity of the adsorbent surface and this model is expressed by equation (4).

$$q_e = K_F C_e^{\,n} \quad (4)$$

According to Temkin isotherm model, it is thought that the surface coverage increases due to the interaction of the

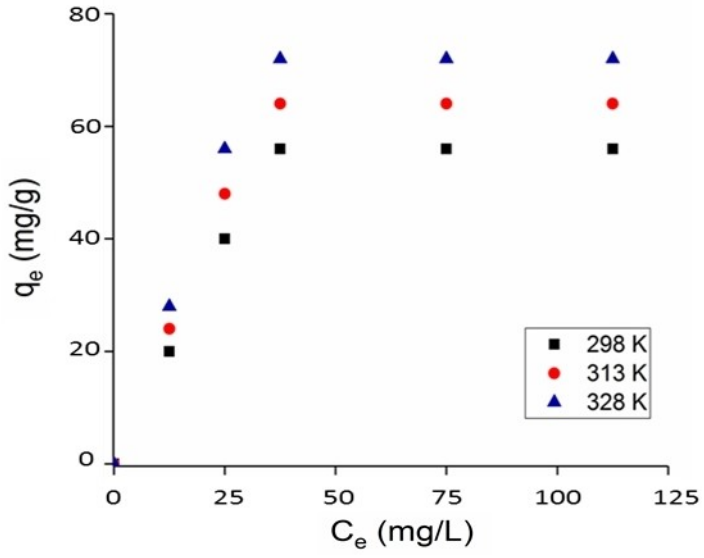

Figure 4. Effect of temperature on the Pb(II) adsorption (adsorption conditions: adsorbent dosage: 25 mg/25 mL, pH = 6, shaking rate 250 rpm and 30 min.).

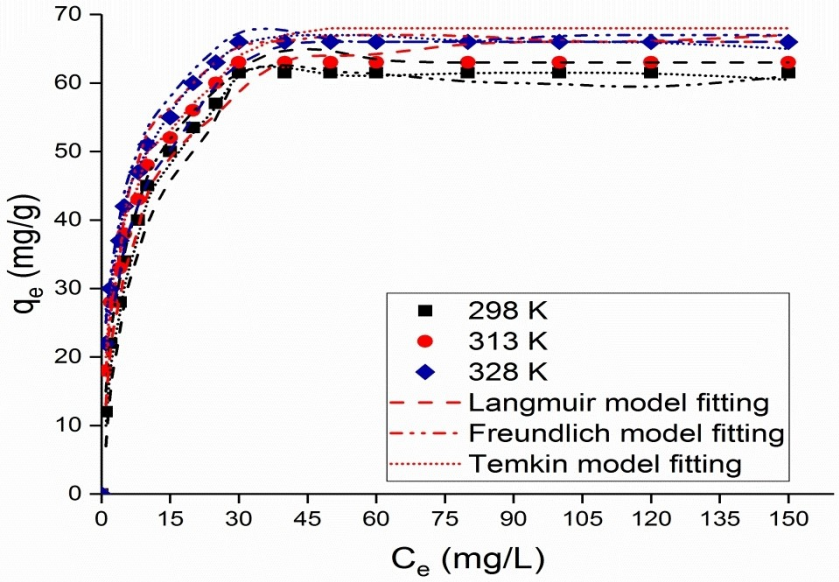

Figure 5. Adsorption isotherm of Pb(II) onto the Fe/Cu–CS adsorbent at different solution temperatures (adsorption conditions: 0.025 g/25 mL Fe/Cu -CS, initial Pb(II) concentration 2–1000 mg/L, pH = 6 and 120 min).

adsorbate and the adsorbent, and as a result, the heat of adsorption of the molecules in the layer decreases linearly. This model is expressed by equation (5).

$$q_e = Bln(K_T C_e) \quad (5)$$

where Ce is the equilibrium concentration of the adsorbate (mg/L), K_L the Langmuir adsorption constant (L/mg), qe is the amount of adsorbate adsorbed per unit mass of adsorbent (mg/g) and qm is the theoretical maximum adsorption capacity (mg/g). n and K_F (L/mg) are Freundlich constants. K_F is defined as an adsorption or distribution coefficient representing the amount of adsorbate adsorbed on an adsorbent for a unit equilibrium concentration while n gives an indication of how favorable the adsorption process. The slope of 1/n ranging between 0 and 1 is a measure of adsorption intensity or surface heterogeneity, becoming more heterogeneous as its value gets closer to zero.[63] B (J/mol) is the Temkin constant related to heat of adsorption and K_T (L/mg) is the equilibrium binding constant. A negative value of B indicates that the adsorption process is endothermic and a positive value of B represents the process is exothermic.[64]

Adsorption kinetics

Determination of kinetic parameters is very important in terms of helping to explain the adsorption mechanism. Two types of kinetic models are commonly used for this purpose; pseudo-first order kinetic model equation (6) and pseudo-second order kinetic model equation (7).

$$\ln(q_e - q_t) = \ln q_e - k_1 t \quad (6)$$

$$\frac{t}{q_t} = \frac{1}{h} + \frac{t}{q_e}, \; h = k_2 q_e^2 \quad (7)$$

The notations q_e and q_t express the amount of Pb(II) adsorbed on Fe/Cu–CS at equilibrium and a specific time t, while k_1 and k_2 are the pseudo-first and pseudo-second order rate constant, respectively. While the graph of t versus $\ln(q_e - q_t)$ drawn according to the calculated values for the pseudo first-order rate expression (equation (6)) is shown in Figure 6(a), the graph of t versus t/q_t drawn according to the calculated values for the pseudo second-order rate expression (equation (7)) is shown in Figure 6(b) at different time intervals of 20 mg/L concentration of Pb(II) adsorption on Fe/Cu–CS beads at 298 K. The kinetic parameters calculated from the slopes and cuts of the lines obtained from these graphs are given in Table 2.

According to these data, the closest correlation value to 1 is Pseudo second order rate kinetics. Therefore, the Fe/Cu–CS nanocomposite is more suitable for pseudo-second order rate kinetics.

Adsorption thermodynamics

The enthalpy change, entropy change, free energy change and equilibrium constant during adsorption are determined and the adsorption phenomenon is investigated thermodynami-

Table 2. Pseudo-first-order and pseudo-second-order model constants for the adsorption of Pb(II) on Fe/Cu–CS.

Pseudo-first-order			Pseudo-second-order		
k_1 (min^{-1})	R^2	q_e	k_2 ($g\,mg^{-1}\,min^{-1}$)	R^2	q_e
0.0207	0.8660	9.37	0.0068	0.9640	14.73

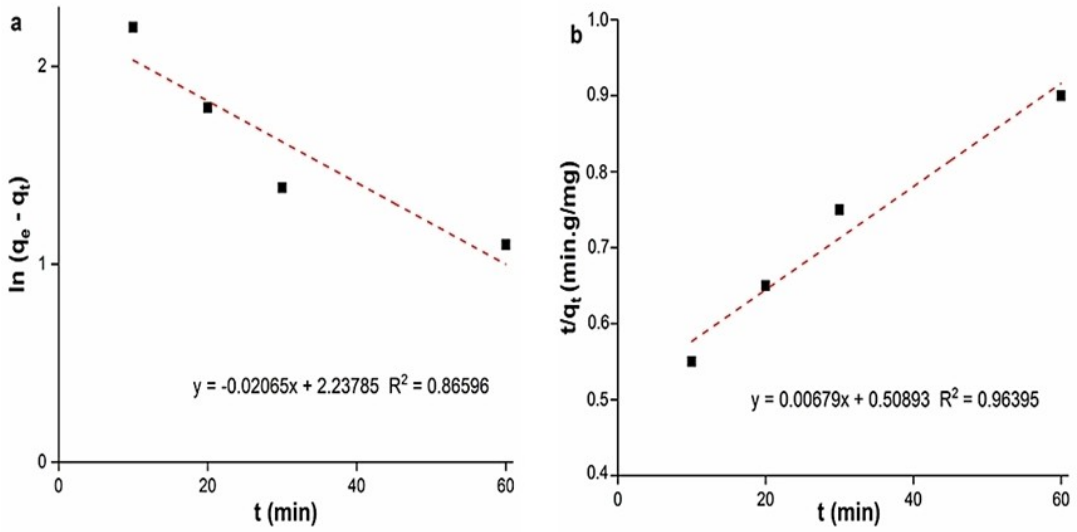

Figure 6. (a) pseudo-first-order and (b) pseudo-second-order kinetic models for adsorption of Pb(II) on Fe/Cu–CS.

cally. The standard free energy of adsorption ΔG°; its standard entropy ΔS°, and its standard enthalpy ΔH°, are calculated from equation (8–10) using the equilibrium constant (K_C) values obtained at various temperatures and are given in Table 3.

$$K_C = \frac{q_e}{C_e} \tag{8}$$

$$\Delta G0 = -RT\ lnKC \tag{9}$$

$$lnK_C = \frac{-\Delta H^0}{R}x\ \frac{1}{T} + \frac{\Delta S^0}{R} \tag{10}$$

where R is the ideal gas constant (R = 8.314 J/molK), K_C represents the equilibrium constant (dimensionless) and T is the absolute temperature (K).

Thermodynamic analysis was performed at three different temperatures (298 K, 313 K and 328 K). The Gibbs free energy was calculated by using equation 9 in which the K_C values were calculated from equation 8. ΔH° and ΔS° values were found by plotting 1/T vs. lnK_C using equation 10 (Van't Hoff equation) and these values are given in Table 3.

The negative and decreasing ΔG° value with temperature shows that the adsorption is spontaneous and the tendency to be spontaneous at higher temperatures increases. The positive ΔH° value indicated that the adsorption was endothermic. The positive ΔS° value showed an increase in the randomness at the adsorbent/solution interface during the adsorption process.

Table 3. Thermodynamic parameters for the adsorption of Pb(II) on Fe/Cu–CS.

ΔG° (kJ mol^{-1})			Van't Hoff Equation	ΔH° (kJ mol^{-1})	ΔS° (J mol^{-1} K^{-1})
298 K	313 K	328 K	y = −965.84x + 10.46	8.03	87.01
−17.9	−19.2	−20.5	R^2 = 0.9791		

Adsorption mechanism

The FT-IR spectra of Fe/Cu–CS for before and after adsorption of Pb (II) ions are comparatively given in Figure 7(a). When the FT-IR spectra of nanoadsorbent and Pb(II) loaded nanoadsorbent were compared, shifts in wave number were observed at certain peaks after Pb(II) adsorption. These are O–H group at 3465 cm^{-1}, –COO group at 1595 cm^{-1}, –O–C–O– ether group at 1417 cm^{-1} and –C–O– alcohol group at 1100 cm^{-1} in the Fe/Cu–CS was shifted to lower wavenumber and narrowed after adsorption of Pb(II). These wave number shifts are caused by ion changes in the specified functional groups due to Pb(II) binding to the nanoadsorbent.[65]

Adsorption mechanisms generally involve the extensive effect of ion exchange, complexation, precipitation, electrostatic and π–π interaction types.[66,67] According to the results of the kinetic and isotherm experiments, chemical adsorption on the monolayer surface played an active role in Pb(II) removal; The main factor is thought to be chemical interaction. Figure 7(b) gives a diagram of the possible chemical interaction mechanism depending on the functional groups.

The comparison of this study with some literature studies on lead removal in terms of adsorption capacity and mechanism is given in Table 4.

Desorption

Recovery/desorption of the adsorbed metal is one of the most important stages of the adsorption process. In order to evaluate the recovery conditions of adsorbed Pb(II) ions, desorption experiments were performed with HNO_3 at different concentrations (1, 3 and 5 mM) and the results in Figure 8(a)

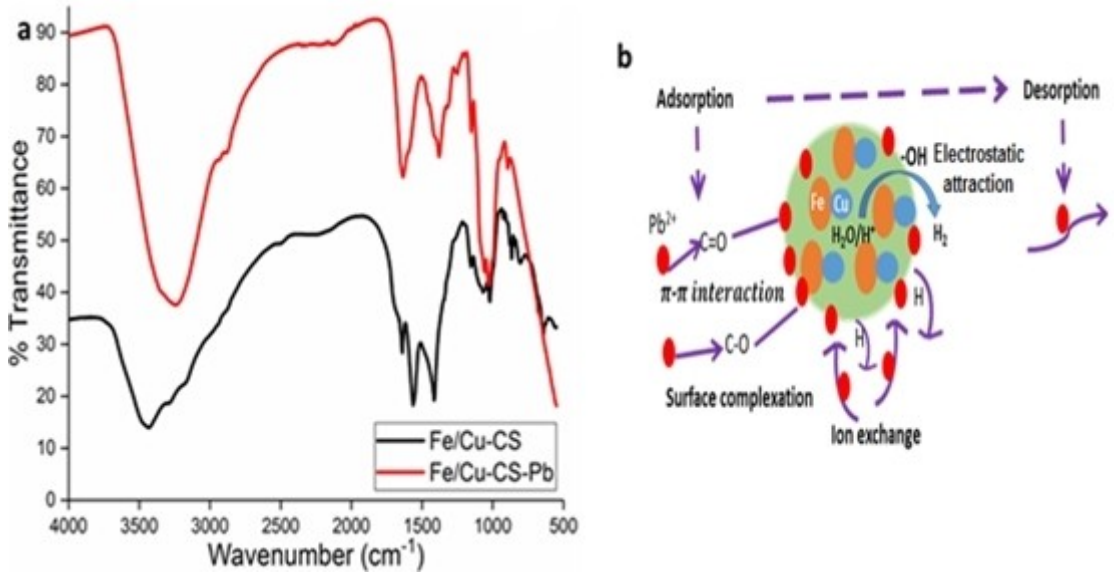

Figure 7. (a) FTIR spectra of Fe/Cu–CS for before and after adsorption of Pb(II) (b) mechanism scheme of Pb sorption by Fe/Cu–CS.

Table 4. A comparison of the adsorptive capacity of the prepared sorbent with those announced in the literature.

Adsorbent	Adsorption Mechanism	Isotherm Model	Kinetic Model	q_m (mg/g)	Contact Time (h)	Reference
Fe_3O_4NPs	Reduction	Temkin	Second	17.30	24	[68]
Banana peels	Electrostatic attraction	Freundlich	Second	247.10	48	[69]
Sludge	Co-precipitation, *complexation*	Freundlich	Second	30.88	4	[70]
Ragweed	Precipitation, ion exchange, *complexation*	Langmuir	Second	358.70	24	[71]
BC-$ZnCl_2$, $FeCl_3$, $FeSO_4$	–	–	–	52.40	48	[72]
BC- KMnO4	Surface adsorption mechanisms	Redlich Peterson	Richie n-th-order	153.10	24	[73]
BC-$FeCl_3 \cdot 6H_2O$, $FeSO_4 \cdot 7H_2O$	Surface complexation, electrostatic attraction, and precipitation	Langmuir	Second	12	127	[74]
Camellia seed husk	Ion exchange, complexation, Pb–π interaction, and precipitation	Langmuir	Second	109.67	48	[75]
Fe/Cu–CS	Electrostatic *attraction*, Ion exchange, surface complexation, Pb–π interaction	Langmuir	Second	61.5	2	Present Study

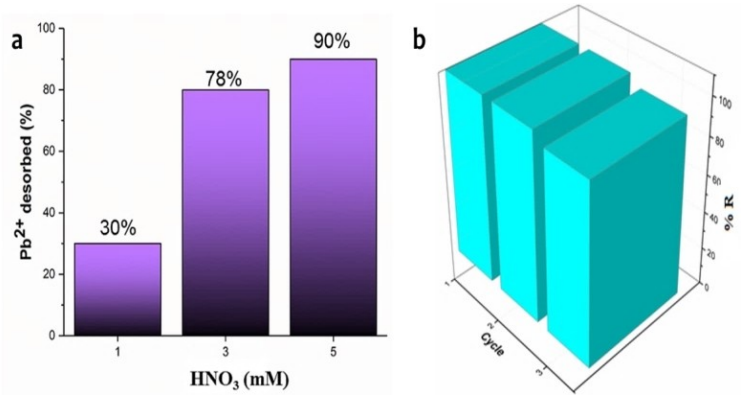

Figure 8. (a) Desorpsiyon of Pb(II) on Fe/Cu–CS (b) effect of cycles on the adsorption/desorption capacity for Pb(II).

were obtained. The mixture was agitated at 250 rpm and 298 K for 2 h. As seen in Figure 8(a), the maximum recovery percentage for Pb(II) ions was obtained with 5 mM HNO_3 (90%). The recovery efficiency, R (%) of Pb(II) from the solid phase was calculated by equation (11):

$$R\,\% = \frac{(C_{des})}{(C_{ads})} * 100 \quad (11)$$

The reusability of Fe/Cu–CS nanoadsorbent was examined by performing 3 cycles at the same concentration, and the results in Figure 8(b) were obtained. As seen, no significant decrease in the adsorption capacity of Fe/Cu–CS nanoadsorbents was observed during the three cycles. The results demonstrated that Fe/Cu–CS nanoadsorbents can be used for the removal and recovery of Pb(II) ions from wastewater over a number of cycles, indicating its suitability for the design of a continuous process.

Adsorption and desorption of Pb(II) at ng/mL level

After these experiments, both 25 mL 50 ng/mL Pb(II) and 25 mL 200 ng/mL Pb(II) solutions were separately prepared to check whether the synthesized nanocomposite material adsorbs Pb(II) ions at lower concentrations. For this, adsorption and desorption studies were repeated at the same optimum experimental conditions (adsorption conditions: adsorbent dosage: 25 mg/25 mL, pH = 6, T = 298 K, shaking rate 250 rpm and 120 min). Since the detection limit of the AAS instrument was insufficient for Pb(II) solutions for both 50 and 200 ng/mL of Pb(II), more sensitive technique, such as ICP-OES with respect to AAS were used in the detection step. Adsorption results showed that 50 and 200 ng/mL Pb(II) ions were adsorbed by nanocomposite at 100% efficiency shown in Table 5. During desorption, 25 mL and 5 mL of 5 mM HNO_3 solutions were used and the adsorbed Pb(II) ions were recovered at about 90% efficiency as similar with 20 mg/L Pb(II) shown in Table 5.

Table 5. Adsorption and desorption efficiency of Pb(II) at ng/mL level on Fe/Cu–CS.

Samples	ICP-OES Results (ng/mL)
1–50 ng/mL Pb (25 *mL*)	51.2 ± 0.5
2–200 ng/mL Pb (25 *mL*)	203.3 ± 2.0
3–50 ng/mL Pb + 25 *mg* Adsorbent (25 *mL*) (Adsorption: 30 min)	< LOD*
4–200 ng/mL Pb + 25 *mg* Adsorbent (25 *mL*) (Adsorption: 30 min)	< LOD*
5–25 *mL* 5 mM HNO_3 for sample 3 (Desorption: 2 h)	46.1 ± 0.5
6–25 *mL* 5 mM HNO_3 for sample 4 (Desorption: 2 h)	183.7 ± 1.8
7–5 *mL* 5 mM HNO_3 for sample 3 (Desorption: 2 h)	256 ± 2.6
8–5 *mL* 5 mM HNO_3 for sample 4 (Desorption: 2 h)	1018 ± 10.2

* Linear Range for ICP-OES for Pb(II): 1 to 500 ng/mL; Limit of Detection (LOD): 0.3 ng/mL

Conclusion

In this study, the usability of green nanoparticles/nanocomposites as an effective and low-cost adsorbent in the removal of one of the toxic heavy metal ions, such as Pb(II) from aqueous solutions by adsorption method was evaluated. The effects of various experimental parameters on the adsorption efficiency were investigated, and the effects of some ions in the tap water on the removal efficiency were investigated and it was observed that the ions in the tap water had no effect on the Pb(II) removal. When the data obtained are evaluated, the optimum aqueous solution pH was determined as 6.0 for the adsorption of Pb(II) ions. It was observed that the adsorption efficiency reached its maximum after 30 minutes of equilibrium time. It was determined that the amount of adsorption increased with increasing initial Pb(II) ions concentration. It has been determined that the adsorbent can be used at least 3 times without being regenerated and 5 mM HNO_3 solution is suitable for desorption of Pb(II) ions. It was observed that the data obtained from the adsorption of Pb(II) ions on Fe/Cu–CS beads were in good agreement with the Langmuir isotherm model, which indicates that the active adsorption sites on the adsorbent surface show a homogeneous distribution. When all these results were evaluated, it was concluded that Fe/Cu–CS beads could be used as an effective and inexpensive adsorbent in removing Pb(II) ions from mg/L to ng/mL level from aqueous solutions by adsorption method. The lathyrus brachypterus endemic plant used in the study was used naturally without any pretreatment requiring chemical reagents, and nanoparticles/nanocomposites were synthesized by green synthesis method. This situation not only reduced the cost of process, but also contributed to green chemistry by preventing the use of chemicals.

Supporting Information Summary

Details of the experimental procedures for the characterizations of nanoparticles/nanocomposites corresponding references are provided in the supporting information.

Acknowledgements

This study was supported by TUBITAK (The Scientific and Technological Research Council of Turkey) 1002-A Projects (122Z830).

Conflict of Interests

The authors have no conflict of interests to declare that are relevant to the content of this article.

Data Availability Statement

The data that support the findings of this study are available from the corresponding author upon reasonable request.

Keywords: Adsorption · Desorption · Green synthesis · Magnetic nanoadsorbents · Pb(II)

[1] S. A. Shammi, A. Salam, M. A. H. Khan, *Environ. Monit. Assess.* **2021**, *193*, 104.
[2] J. Briffa, E. Sinagra, R. Blundell, *Heliyon* **2020**, *6*, e04691.
[3] F. A. C. Amorim, S. L. C. Ferreira, *Talanta* **2005**, *65*, 960–964.
[4] A. Saravanan, P. S. Kumar, P. R. Yaashikaa, S. Karishma, S. Jeevanantham, S. Swetha, *Chemosphere* **2021**, *277*, 130236.
[5] A. B. Rakhym, G. A. Seilkhanova, T. S. Kurmanbayeva, *Mater. Today: Proc.* **2020**, *31*, 482–485.
[6] F. Xie, X. Lin, X. Wu, Z. Xie, *Talanta* **2008**, *74*, 836–843.
[7] X.-M. Zhan, X. Zhao, *Water Res.* **2003**, *37*, 3905–3912.
[8] R. V. Hemavathy, A. Saravanan, P. S. Kumar, D. V. N. Vo, S. Karishma, S. Jeevanantham, *Chemosphere* **2021**, *283*, 131276.
[9] Ş. Taşar, F. Kaya, A. Özer, *J. Environ. Chem. Eng.* **2014**, *2*, 1018–1026.
[10] G. García-Rosales, A. Colín-Cruz, *J. Environ. Manage.* **2010**, *91*, 2079–2086.
[11] Y. Bulut, Z. Baysal, *J. Environ. Manage.* **2006**, *78*, 107–113.
[12] E. Y. Danish, H. M. Marwani, K. F. Almoslehi, E. M. Bakhsh, *Environ. Sci. Pollut. Res. Int.* **2020**, *27*, 5408–5417.
[13] J. Li, X. X. Wang, G. X. Zhao, C. L. Chen, Z. F. Chai, A. Alsaedi, T. Hayatf, X. K. Wang, *Chem. Soc. Rev.* **2018**, *47*, 2322–2356.
[14] S. T. Hussain, S. A. Khaleefa Ali, *J. Ecol. Eng.* **2020**, *22*, 104–111.
[15] Y. D. Zou, X. X. Wang, A. Khan, P. Y. Wang, Y. H. Liu, A. Alsaedi, T. Hayat, X. K. Wang, *Environ. Sci. Technol.* **2016**, *50*, 7290–7304.
[16] N. Meunier, P. Drogui, C. Montane, R. Hausler, G. Mercier, J. F. Blais, *J. Hazard. Mater.* **2006**, *137*, 581–590.
[17] A. Benhamou, M. Baudu, Z. Derriche, J. P. Basly, *J. Hazard. Mater.* **2009**, *171*, 1001–1008.
[18] S. Kaushal, N. Kaur, M. Kaur, P. P. Singh, *J. Photochem. Photobiol. A* **2020**, *403*, 112841.
[19] G. X. Zhao, X. B. Huang, Z. W. Tang, Q. F. Huang, F. L. Niu, X. K. Wang, *Polym. Chem.* **2018**, *9*, 3562–3582.
[20] M. E. Malool, M. Keshavarz Moraveji, J. Shayegan, *J. Taiwan Inst. Chem. Eng.* **2022**, *133*, 104203.
[21] X. Qu, P. J. J. Alvarez, Q. Li, *Water Res.* **2013**, *47*, 3931.
[22] P. Panneerselvam, N. Morad, K. A. Tan, *J. Hazard. Mater.* **2011**, *186*, 160–168.
[23] R. K. Gautam, P. K. Gautam, S. Banerjee, S. Soni, S. K. Singh, M. C. Chattopadhyaya, *J. Mol. Liq.* **2015**, *204*, 60–69.
[24] F. T. Fato, D.-W. Li, L.-J. Zhao, K. Qiu, Y.-T. Long, *ACS Omega* **2019**, *4*, 7543–7549.
[25] H. Baseri, S. Tizro, *Process Saf. Environ. Prot.* **2017**, *109*, 465–477.
[26] M. Sundararajan, L. J. Kennedy, P. Nithya, J. J. Vijaya, M. Bououdina, *J. Phys. Chem. Solids* **2017**, *108*, 61–75.
[27] S.-H. Lee, H. Choi, K.-W. Kim, *J. Geochem. Explor.* **2018**, *184*, 247–254.
[28] G. Neeraj, S. Krishnan, P. S. Kumar, K. R. Shriaishvarya, V. Vinoth Kumar, *J. Mol. Liq.* **2016**, *214*, 335–346.
[29] Y.-R. Zhang, S.-Q. Wang, S.-L. Shen, B.-X. Zhao, *Chem. Eng. J.* **2013**, *233*, 258–264.
[30] J. Chang, Z. Zhong, H. Xu, Z. Yao, R. Chen, *Chin. J. Chem. Eng.* **2013**, *21*, 1244–1250.
[31] L. Shi, X. Zhang, Z. Chen, *Water Res.* **2011**, *45*, 886892.
[32] N. Pandey, S. K. Shukla, N. B. Singh, *Adv. Mater. Lett.* **2015**, *6*, 172178.
[33] Y. Babaee, C. N. Mulligan, M. S. Rahaman, *J. Chem. Biotechnol.* **2018**, *93*, 6371.
[34] Z. Li, S. Deng, G. Yu, J. Huang, V. C. Lim, *Chem. Eng. J.* **2010**, *161*, 106113.
[35] S. Lata, S. R. Samadder, *J. Environ. Manage.* **2016**, *166*, 387406.
[36] M. Şahin, Y. Arslan, F. Tomul, B. Yıldırım, H. Genç, *React. Kinet. Mech. Catal.* **2022**, *135*, 3303–3315.
[37] M. Şahin, Y. Arslan, F. Tomul, *Res. Chem. Intermed.* **2022**, *48*, 5209–5226.
[38] M. Şahin, Y. Arslan, F. Tomul, *Int. J. Environ. Anal. Chem.* **2022**, doi: 10.1080/03067319.2022.2140417.
[39] M. Baghayeri, B. Mahdavi, Z. H. M. Abadi, S. Farhadi, *Appl. Organometal Chem.* **2018**, *32*, 4057.
[40] S. G. Balwe, V. V. Shinde, A. A. Rokade, S. S. Park, Y. T. Jeong, *Catal. Commun.* **2017**, *99*, 121–126.
[41] S. Logpriya, V. Bhuvaneshwari, D. Vaidehi, R. P. Senthil Kumar, R. S. N. Malar, B. P. Sheetal, R. Amsaveni, M. Kalaiselvi, *J. Nanostructure Chem.* **2018**, *8*, 301.
[42] A. Chaudhry, F. Bashir, S. F. Adil, S. Saif, M. R. Shaik, M. R. Hatshan, B. Shaik, *J. King Saud Univ. Sci.* **2022**, *34*, 101927.
[43] M. Kragović, M. Stojmenović, J. Petrović, J. Loredo, S. Pašalić, A. Nedeljković, I. Ristović, *Procedia Manuf.* **2019**, *32*, 286.
[44] M. Kumari, C. U. Pittman Jr, D. Mohan, *J. Colloid Interface Sci.* **2015**, *442*, 120.
[45] C. Yuwei, W. Jianlong, *Chem. Eng. J.* **2011**, *168*, 286.
[46] M. Danish, X. Gu, S. Lu, A. Ahmad, M. Naqvi, U. Farooq, X. Zhang, X. Fu, Z. Miao, Y. Xue, *Chem. Eng. Sci.* **2017**, *308*, 396.
[47] S. Hussain, M. Kamran, S. A. Khan, K. Shaheen, Z. Shah, H. Suo, Q. Khan, A. B. Shah, W. U. Rehman, Y. O. Al-Ghamdi, U. Ghani, *Int. J. Biol. Macromol.* **2021**, *168*, 383.
[48] N. Illy, M. Robitzer, R. Auvergne, S. Caillol, G. David, B. Boutevin, *J. Polym. Sci. A: Polym. Chem.* **2013**, *52*, 39.
[49] A. Mohammadi, H. Daemi, M. Barikani, *Int. J. Biol. Macromol.* **2014**, *69*, 447.
[50] Z. Ayazi, Z. M. Khoshhesab, F. F. Azhar, Z. Mohajeri, *J. Chin. Chem. Soc.* **2017**, *64*, 627.
[51] L. Yang, X. Ma, N. Guo, *Carbohydr. Polym.* **2012**, *90*, 853.
[52] C. Gkanatsiou, N. Ntalli, U. Menkissoglu-Spiroudi, C. Dendrinou-Samara, *J. Nanotechnol. Res.* **2019**, *1(2)*, 43.
[53] I. Othman, M. Abu Haija, F. Banat, *J. Nanomater.* **2019**, *2019*, 1.
[54] H. D. Omar, *Int. Lett. Chem. Phys. Astron.* **2016**, *64*, 130.
[55] Y. Babaee, C. N. Mulligan, Md. S. Rahaman, *Environ. Earth Sci.* **2017**, *76*, 650.
[56] W. Yantasee, C. L. Warner, T. Sangvanich, R. S. Addleman, T. G. Carter, R. J. Wiacek, G. E. Fryxell, C. Timchalk, M. G. Warner, *Environ. Sci. Technol.* **2007**, *41*, 5114.
[57] Z. Sheikh, M. Amin, N. Khan, M. N. Khan, S. K. Sami, S. B. Khan, I. Hafeez, S. A. Khan, E. M. Bakhsh, C. K. Cheng, *Chemosphere* **2021**, *279*, 130545.
[58] D. Lv, J. Zhou, Z. Cao, J. Xu, Y. Liu, Y. Li, K. Yang, Z. Lou, L. Lou, X. Xu, *Chemosphere* **2019**, *224*, 306–315.
[59] N. Melitas, O. Chuffe-Moscoso, J. Farrell, *Environ. Sci. Technol.* **2001**, *35*, 3948–3953.
[60] N. Kataria, V. K. Garg, *Chemosphere* **2018**, *208*, 818–828.
[61] I. A. Mohammed, A. H. Jawad, A. S. Abdulhameed, M. S. Mastuli, *Int. J. Biol. Macromol.* **2020**, *161*, 503–513.
[62] M. Peydayesh, A. Rahbar-Kelishami, *J. Ind. Eng. Chem.* **2014**, *21*, 1014–1019.
[63] K. Fytianos, E. Voudrias, E. Kokkalis, *Chemosphere* **2000**, *40*, 3.
[64] P. Paluri, K. A. Ahmad, K. S. Durbha, *Biomass Conv. Bioref.* **2022**, *12*, 4031–4048.
[65] Q. Wang, Y. Wang, Z. Yang, W. Han, L. Yuan, L. Zhang, X. Huang, *Chem. Eng. J. Adv.* **2022**, *11*, 100295.
[66] G. X. Yang, H. Jiang, *Water Res.* **2014**, *48*, 396–405.
[67] H. Jin, M. U. Hanif, S. Capareda, Z. Chang, H. Huang, Y. Ai, *J. Environ. Chem. Eng.* **2016**, *4(1)*, 365–372.
[68] S. T. Neeli, H. Ramsurn, C. Y. Ng, Y. Wang, J. Lu, *J. Environ. Chem. Eng.* **2020**, *8*, 103886.
[69] Z. Ahmad, B. Gao, A. Mosa, H. Yu, X. Yin, A. Bashir, H. Ghoveisi, S. Wang, *J. Cleaner Prod.* **2018**, *180*, 437–449.
[70] H. Lu, W. Zhang, Y. Yang, X. Huang, S. Wang, R. Qiu, *Water Res.* **2012**, *46*, 854–862.
[71] W. Lian, L. Yang, S. Joseph, W. Shi, R. Bian, J. Zheng, L. Li, S. Shan, G. Pan, *Bioresour. Technol.* **2020**, *317*, 124011.
[72] S.-Y. Wang, Y.-K. Tang, C. Chen, J.-T. Wu, Z. Huang, Y.-Y. Mo, K.-X. Zhang, J.-B. Chen, *Bioresour. Technol.* **2015**, *186*, 360–364.
[73] H. Wang, B. Gao, S. Wang, J. Fang, Y. Xue, K. Yang, *Bioresour. Technol.* **2015**, *197*, 356–362.
[74] X. Huang, D. Wei, X. Zhang, D. Fan, X. Sun, B. Du, Q. Wei, *Sci. Total Environ.* **2019**, *685*, 681–689.
[75] J. Wu, T. Wang, Y. Zhang, W. P. Pan, *Bioresour. Technol.* **2019**, *291*, 121859.

Submitted: February 23, 2023
Accepted: April 21, 2023